Journal of the European Ceramic Society 39 (2019) 3353–3363

Contents lists available at ScienceDirect

Journal of the European Ceramic Society

journal homepage: www.elsevier.com/locate/jeurceramsoc

Original article

Advancing the fabrication of YSZ-inverse photonic glasses for broadband omnidirectional reflector films

Jefferson J. do Rosário[a], Yen Häntsch[a], Robert M. Pasquarelli[a], Pavel N. Dyachenko[b], Eleonora Vriend[a,c], Alexander Yu Petrov[b,d], Kaline P. Furlan[a], Manfred Eich[b], Gerold A. Schneider[a,*]

[a] Institute of Advanced Ceramics, Hamburg University of Technology, Denickestrasse 15, 21073, Hamburg, Germany
[b] Institute of Optical and Electronic Materials, Hamburg University of Technology, Eissendorfer Strasse 38, 21073, Hamburg, Germany
[c] Department of Materials Science, University of Cambridge, 27 Charles Babbage Road, Cambridge, CB3 0FS, UK
[d] ITMO University, 49 Kronverkskii Ave., 197101, St. Petersburg, Russia

ARTICLE INFO

Keywords:
Photonic glass
Yttrium-stabilized zirconia (YSZ)
Broadband omnidirectional reflector
High-temperature photonics
Thermal barrier coating (TBC)

ABSTRACT

A single-step and all-colloidal deposition method to fabricate yttrium-stabilized zirconia (YSZ)-inverse photonic glasses with 3 µm pores was developed. The process is based on electrostatic attraction and repulsion in suspension, controlled by surface charge of polystyrene (PS) microspheres and YSZ nanoparticles, used as pore templates and matrix material, respectively. The pH was used as a tool to change surface charges and particle-particle interactions. Photonic glass films with 3 µm pores yielded broadband omnidirectional reflection over the wavelengths of 1–5 µm, relevant for thermal radiation at temperatures around 1200 °C. These highly porous materials maintained their structural stability and reflectance after being annealed at 1200 °C for 120 h.

1. Introduction

Since García et al. [1] presented the concept of the photonic glass in 2007 much has been done in this field of disordered photonics. Various applications have been developed, from random lasing [1–3] and resonance-dependent Anderson localization [1,2], proposed back then, to broadband omnidirectional reflectors [4–6] and structural colorations [7–9].

We have been developing refractory photonic glasses for the next-generation of thermal barrier coatings (TBCs) in order to reduce the heat transfer at turbine blades by thermal conduction and effectively reflect thermal radiation. The heat conduction is reduced due to the high porosity and low conduction pathways. The high diffuse reflectance over a broad wavelength range is the result of multiple scattering created in these disordered systems. Because the radiative contribution, with T^4 dependency, becomes increasingly significant as the gas inlet temperature of a gas turbine increases [10], the reflection of thermal radiation in TBCs also becomes more important. The concept based on multi-stacks of photonic crystals by Lee et al. [11] shows that in the relevant temperature of 1200 °C the coverage of most of the black body radiation spectrum (wavelengths from 1–5 µm) may require up to 10 stacks of photonic crystals with different lattice constants, because the reflection bands of photonic crystals with a single pore size are rather narrow. Instead, photonic glasses have been shown to be more suitable for broadband reflectors than multi-stacks photonic crystals [4]. Disordered structures offer the advantage of broadband omnidirectional reflectance which could eliminate the need for depositing multi-layer coatings and their photonic performance is virtually insensitive to structural flaws.

As in photonic crystals, the wavelengths reflected by photonic glasses are dependent on the particle or pore size. However, the particle or pore size does not determine the wavelength with maximum reflection but the broadband cutoff wavelength. The absolute reflectance can be increased by varying the particle/pore size or by increasing the refractive index contrast, the amount of high refractive index material in the final structure and the film thickness. We use yttria-stabilized zirconia (YSZ), known from TBC applications, as the material of choice due to its phase stability, high refractive index of 2.1, optical transparency from visible to 5 µm and low thermal conductivity [10]. The reflection of radiation in the infrared wavelength range of 1–5 µm is a benchmark [11], and has been achieved for direct photonic glasses fabricated by sedimentation of zirconia [5] and yttria-stabilized zirconia (YSZ) [6] microspheres with diameters up to 4 µm. In the work of Dyachenko et al. [5], simulations have shown that for zirconia direct

* Corresponding author.
E-mail address: g.schneider@tuhh.de (G.A. Schneider).

https://doi.org/10.1016/j.jeurceramsoc.2019.04.028
Received 3 April 2019; Accepted 12 April 2019
Available online 15 April 2019

photonic glasses, microparticles with a size of around 3 μm are required to achieve the coverage of the desired wavelength range. Ceramic photonic glasses [4–6] have shown larger coverage of wavelengths compared to multistack ceramic photonic crystals using materials such as TiO_2 [12,13], SiO_2 [14,15] and composites of SiO_2-TiO_2 [15] and Al_2O_3-ZnO-TiO_2 [16]. It should be mentioned that none of these materials are suitable for high-temperature applications. Additionally, inverse photonic glasses, which are based on pores dispersed in a ceramic matrix, require further development.

Towards the fabrication of YSZ-based, inverse photonic glass films with pores bellow 1 μm, we recently developed an all-colloidal and single-step deposition method [4] based on previous work with alumina [17] and YSZ nanoparticles [18,19]. This method relies on the heterocoagulation of positively charged YSZ nanoparticles ($d \sim 10$ nm) and negatively charged monodispersed polymer microspheres ($d = 756$ nm) in an aqueous suspension. Heterocoagulation results from the mutual attraction of particles carrying opposite surface charges in suspension. The mixture of these particles induces the formation of a ceramic shell on the surface of the polymer spheres. After sedimentation of the suspension and drying, the polymer template can be removed by calcination, resulting in a structure composed of ceramic shells. By changing the amount of high refractive index material and varying the film thickness, integrated reflectance of approximately 70% has been obtained in the wavelengths range of 0.4–2.2 μm for a film thickness of less than approx. 40 μm. While the small size of the spherical pores did not yield reflection at the wavelength range desired for TBCs, it agreed relatively well with the range reflected by direct photonic glasses fabricated with 0.67 μm zirconia microspheres [5]. In order to extend the broadband reflection range of YSZ-inverse photonic glasses into the infrared, larger polymer template spheres are required. The creation of a core-shell prior to deposition (in suspension) is important to assure homogeneity of the deposited structure and, to avoid the presence of free nanoparticles that can phase separate from the core-shell polymer-YSZ spheres during deposition. Unfortunately, these criteria become difficult to meet, as larger polymer spheres tend to result in lower amounts of nanoparticles heterocoagulated on their surfaces.

In this work, we present the fabrication of YSZ-inverse photonic glasses with larger pores (using template polymer spheres larger than 3 μm) in a single-step and all-colloidal deposition method. We determine the limit of heterocoagulation for this template particle size and show how to increase the infiltration of the final structure by varying the pH of the suspension to control particle charges, agglomeration and sedimentation. The DLVO (Derjaguin, Landau, Verwey, and Overbeek) theory [20–22] is used to explain the interactions of particles under different deposition conditions. Final structures with a high filling fraction of YSZ and high reflectance over the desired wavelength range were achieved. In addition, these structures exhibited structural stability and maintained their reflectance behavior up to the desired temperature of 1200 °C for up to 120 h.

2. Materials and methods

As base materials, commercial monodispersed polystyrene (PS) spheres with a diameter of 3.21 μm ± 0.07 μm (Microparticles GmbH) and YSZ (zirconia doped with 8 mol % yttria) nanopowder (Sigma Aldrich) with a particle size of ≤ 100 nm and crystallite sizes of 5–10 nm were used. The YSZ nanopowder was dispersed in deionized water in a ball mill with zirconia milling spheres.

Suspensions were prepared in deionized water by mixing stock suspensions of the PS spheres (100 mg mL^{-1}) and YSZ (300 mg mL^{-1}). The concentration of PS spheres was maintained constant at 20 mg mL^{-1}, and the concentration of YSZ nanoparticles was varied at 4, 6, 8, 10, 20, 30, 40 and 50 mg mL^{-1}. These concentrations resulted in YSZ/PS ratios of 0.2, 0.3, 0.4, 0.5, 1.0, 1.5, 2.0 and 2.5 by weight. The mixtures were ultrasonicated for 30 min to homogenize the suspension and to promote interaction between polymer and ceramic particles. The pH of the suspensions was varied from a starting pH of 6–8 and 10 by adding an aqueous KOH solution (0.1 M). After the desired pH was achieved the suspensions were again ultrasonicated for 30 min for homogenization. Suspensions were drop-casted within a silicon ring fixed to a cleaned, hydrophilic soda-lime silica glass substrate or to a sapphire single-crystal substrate, the later used mostly for high temperature investigations. The substrates were cleaned by soaking in an alkaline detergent solution (Mucasol, Merz Hygiene GmbH) for several hours in an ultrasonic bath, brushing, rinsing subsequently with hot tap water and with deionized water, and blow dried by filtered nitrogen. Due to the fixed silicon ring, the resulting area of the sample was 4.5 cm^2. The amount of suspension deposited was 300 μL for each sample. Samples were left to dry at room temperature overnight covered with a glass vessel. Dried, as-cast samples were annealed at 500 °C for 30 min in air at a heating rate of 1 °C min^{-1} to remove the polymeric template, yielding the inverse structure. In order to investigate their temperature stability, inverse structures deposited on sapphire were sequentially annealed at 1000 °C for 1 h, at 1200 °C for a total of 1, 4, 24 and 120 h at a heating rate of 5 °C min^{-1}.

Zeta potentials and particle size distributions were measured using a Zetasizer Nano S (Malvern Instruments). For zeta potential measurements, pH titration was performed with an automated titrator using HCl and NaOH solutions (0.25 M). Dilute suspensions were prepared from the stock suspensions of the initial materials. For particle size determination, the different suspensions were prepared at controlled pH values and concentrations (20 mg mL^{-1} for PS and 50 mg mL^{-1} for YSZ, otherwise stated) and then diluted right before the measurements by light stirring in a large volume of deionized water adjusted to the same pH as the suspension being diluted.

The sedimentation behavior was characterized by the clarification thickness of 5 mL of suspension in a glass vessel as a function of time at pH values of 6, 8 and 10. The vessel containing the suspension was graded with a mm scale to help guide the measurement. The concentrations of PS and YSZ suspensions were 20 and 50 mg mL^{-1}, respectively.

The microstructures of the films and their thickness were observed by scanning electron microscopy (SEM, Leo 1530 and Zeiss Supra 55 V P, Carl Zeiss). X-ray diffraction (XRD) was performed using a Cu-Kα radiation source with a LynxEye detector in 1D mode and pseudo-Bragg-Brentano geometry (Bruker AXS D8 Discover). XRD diffractograms were matched to Powder Diffraction Files (PDF) from the International Centre for Diffraction Data (ICDD). A Fourier-transform infrared (FTIR) spectrometer (Vertex 70, Bruker) with a gold-coated integrating sphere accessory was used to measure the hemispherical reflectance between wavelengths of 1 μm and 5 μm.

DLVO (Derjaguin, Landau, Verwey, and Overbeek) theory [20–22] describes the interaction between colloidal particles. The full detailed approach used in this work can be found in the work by Trefalt et al. [23]. The theory approximates the interaction free energy per unit area as the sum of two contributions: van der Waals attraction (W_{vdw}) and electrostatic double layer interactions (W_{dl}):

$$W(h) = W_{vdw}(h) + W_{dl}(h) \quad (1)$$

where h is the separation distance of the particles.

The van der Waals interaction per unit area between two plates is given by $W_{vdw}(h) = -H/12\pi h^2$, where H is the Hamaker's constant, chosen to be 5×10^{-21} J [23]. The double layer contribution is more complex as charge regulation effects need to be taken into account. When two particles approach, the surface charge and potential vary due to ion adsorption, affecting the interactions. A charge regulation parameter, p, taking values between $-\infty$ and 1, is used to describe this effect. The interaction free energy for the double layer is then given by [23]:

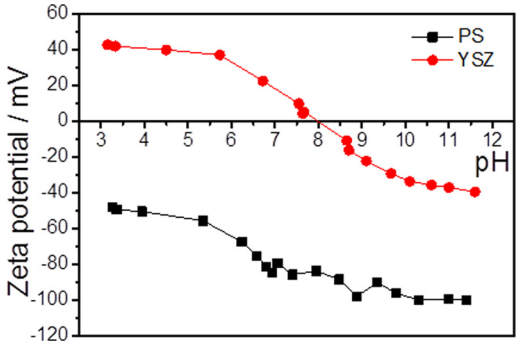

Fig. 1. Zeta potential versus pH for PS and YSZ particles.

$$W_{dl}(h) = \varepsilon\varepsilon_0\kappa\frac{2\Psi_+\Psi_- e^{-\kappa h} + [(2p_+ - 1)\,\Psi_-^2 + (2p_- - 1)\,\Psi_+^2]\,e^{-2\kappa h}}{1 - (2p_+ - 1)(2p_- - 1)e^{-2\kappa h}} \quad (2)$$

where Ψ is the surface potential of the particle, ε_0 is the dielectric permittivity of vacuum, ε is the dielectric constant of the medium (water) taken to be 80, κ is the inverse Debye length and the signs $\pm$ refer to the particles situated on either side at a distance $\pm h/2$. The Debye length κ^{-1} is given by:

$$\kappa^{-1} = \left(\frac{k_B T\varepsilon_0\varepsilon}{2q^2 N_A I}\right)^{1/2} \quad (3)$$

where q is the elementary charge, N_A is the Avogadro's number, I is the ionic strength, k_B is the Boltzmann constant, and T is the absolute temperature.

Given that it is not possible to assess the surface potential for most common situations, the measured zeta potential values (Fig. 1) were used as an approximation for the used surface potentials as given in Table 1. The ionic strength used to calculate the Debye length was estimated by considering the added amount of KOH solution and the final pH of the suspensions being 10^{-6} M, 2×10^{-6} M and 10^{-4} M for pH 6, 8 and 10, respectively.

The two cases typically considered are constant charge (CC), where $p = 1$, and constant potential (CP), where $p = 0$. Although these boundary conditions are useful references, they do not provide the best approximation as the surface charge and potential are unlikely to remain constant as the particles approach each other. Instead, a constant regulation (CR) boundary condition, where p is between 0 and 1, gives a more accurate description [24,25]. The exact value of p can be determined using techniques such as AFM [24,25]. However, for the purpose of our calculations a value of $p = 0.5$ was used for the CR approximation. The charge regulation is related to adsorption of ions on the surface and its extent can vary upon approach.

The force (F) between the particles is calculated with the Derjaguin approximation by $F = 2\pi R_{eff} W(h)$. R_{eff} is the effective particle radius, $R_{eff} = (R_1R_2)/(R_1+R_2)$, R_1 and R_2 being the radius of the different particles in consideration. The interaction free energy (U) of the two particles is finally calculated by integrating

$$U(h) = \int_h^\infty F(h)dh \quad (4)$$

The particle sizes used for the force calculations were extracted from the particle size measurements of YSZ for each pH, and in the case of bimodal particle distributions, the most intense peak was used being

Table 1
Surface potentials of PS- and YSZ-particles at different pHs used for the DLVO calculations.

pH	6	8	10
Ψ_{PS} [mV]	+35	0	−33
Ψ_{YSZ} [mV]	−65	−85	−98

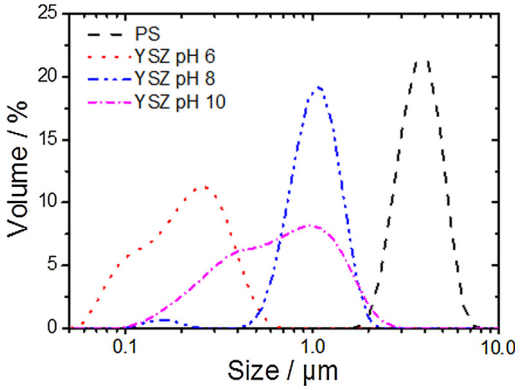

Fig. 2. Particle size distribution of PS- and YSZ-particles at different pHs. The measured volume (%) versus particle size (µm) shows a strong pH-dependence for the YSZ particles. For PS particles there is no pH-dependence of the size.

260 nm, 970 nm and 960 nm for pH 6, 8 and 10, respectively (see Fig. 2). It was assumed that the particles are spherical and their size corresponds to their diameter $2R$.

Optical simulations were performed using the finite-difference time-domain method (FDTD), implemented as a freely available software package Meep [26] with a resolution of 32 pixels per lattice spacing. The reflectance was calculated by modeling the propagation of an incident plane wave at normal incidence. The FDTD calculation region spanned 20 µm × 20 µm size in the x − y plane, with periodic boundary conditions at the sides. Along the z-axis direction at the top and bottom of the simulation structure, perfectly-matched layer boundary conditions were imposed. The thickness of the photonic glass is L along z − axis direction. The refractive index of the YSZ is assumed as $n = 2.12$. All calculated disordered structures have 38% porosity. Models of random structures were obtained using event-driven molecular dynamics simulations of a monodisperse hard sphere system implemented as a freely available software package DynamO [27].

3. Results and discussion

3.1. Materials and suspensions

In order to understand the contributions of the colloidal nature of the particle suspensions on the resulting microstructure of the films, the behavior of the base materials and suspensions was first characterized with respect to their charges, particle sizes, and sedimentation in solution as a function of pH. Zeta potential measurements of the two base materials over a pH range from around 3–11.6 can be seen in Fig. 1. PS spheres dispersed in deionized water exhibited a native pH of 6.5 and a zeta potential of around −75 mV. PS spheres maintained a negative zeta potential over the entire measured pH range with −48 mV at pH 3.2 and −100 mV at pH 11.4. In contrast, the YSZ-nanopowder dispersed in deionized water exhibited a pH of 5.7 and a zeta potential of around +37 mV. The isoelectric point (IEP) was found to occur at pH ~ 8. Maximum and minimum zeta potential values were found at the extremes of the measured pHs, being +42 mV at pH 3.2 and −39 mV at pH 11.6. Simply dispersing the two materials individually in deionized water resulted in stable stock suspensions. The mixing of these stock suspensions led to a mixture with pH ~ 6. The opposite charges of both colloids at this pH resulted in heterocoagulation, as presented in our previous work [4]. The small, positively charged YSZ particles form a shell around the larger, negatively charged PS spheres. It was previously observed [4] that the heterocoagulated shell cannot grow indefinitely and that, during deposition, remaining free YSZ-nanoparticles can phase separate from the PS-YSZ core-shell particles that formed in suspension. The maximum YSZ/PS ratio at which a fully heterocoagulated shell forms changes with the PS template size,

presumably due to the difference in surface area. Increasing the size of the PS leads to a lowering of the maximum YSZ/PS ratio at which complete heterocoagulation occurs and thus a lower filling fraction of solid phase after inversion. The lower YSZ/PS ratio of heterocoagulation becomes a problem for the fabricated photonic glasses, as the magnitude of the reflectance is dependent on the amount of high refractive index material in the structure. In order to overcome such limitations of heterocoagulation in these systems, the pH of the suspension was adjusted in order to change the colloidal interactions. By the modification of the surface charges, agglomeration behavior and sedimentation rates, more favorable interactions for filling the void space between PS particles were identified.

Based on the zeta potential titration curves of the base materials (Fig. 1), three pHs were chosen for this study: the native pH of 6 of the as prepared suspension (PS: −65 mV, YSZ: +35 mV), an adjusted pH of 8 (PS: −85 mV, YSZ: 0 mV) and an adjusted pH of 10 (PS: −98 mV, YSZ: −33 mV). These pHs were chosen because they are the extreme charge cases in the PS-YSZ system: negative-positive, negative-neutral and negative-negative zeta potential pairings, respectively.

Particle size analysis (Fig. 2) was performed to characterize the base materials and to observe the influence of the pH on the agglomeration behavior of the YSZ particles. The curves represent the hygroscopic sizes of the colloids, which is larger than the physical dimensions of the particles that one might determine by other methods, e.g. SEM. The presented curve for PS corresponds to pH 6, with peak position at 3.58 µm. As the PS remained negatively charged over the pH range tested (and thus stabilized by repulsive forces), no distinguishable difference in PS size was observed at different pHs. However, as the YSZ exhibited different surface charges at different pHs, this had a large effect on the particle size. The YSZ nanoparticles at pH 6 presented a bimodal distribution with two peaks at ~0.10 µm and ~0.25 µm. The first peak corresponds to the actual particle size close to the one given by the supplier and the second one to the agglomeration of particles. Complete deagglomeration of the particles could be achieved by introducing a dispersant, but this approach was not followed to avoid influencing the particle charges and interactions by the dispersant. By changing the pH to 8 strong agglomeration of the YSZ nanoparticles was observed. A peak at ~0.95 µm shows large agglomerates due to strong attraction between the non-charged YSZ nanoparticles. Nevertheless, a small peak can be observed at ~0.15 µm showing the presence of a small amount of only slightly agglomerated nanoparticles. By going further to pH 10 the YSZ nanoparticles became negatively charged and were redispersed in the solvent. The peak at ~0.95 µm found at pH 8 decreased to less than half of its intensity and a new peak at ~0.40 µm appeared. The zeta potential of −33 mV of the YSZ at pH 10 is in the limit of colloidal stability, so agglomeration should not take place (at least not up to 1 µm). Nevertheless, the charges and the dispersion process are not enough to completely break apart the agglomerates formed when passing through the IEP at pH 8.

Lastly, the sedimentation behavior of the suspensions at different pHs was quantified by the clarification thickness as a function of time (Fig. 3). The discussion comprises their behavior within 24 h. At pH 6 it can be observed that the PS sediments to its maximum within one hour, while the YSZ shows no clarification. Both colloids are stable at this pH but the difference in size controls the sedimentation. At pH 8 the clarification rates of both suspensions are much closer, being 1.0 and 0.6 mm h^{-1} for PS and YSZ, respectively. The increase in the sedimentation rate of YSZ from pH 6–8 is easily explained by the increased particle size due to the neutral zeta potential, causing agglomeration. The difference in sedimentation rate of PS between pH 6 and pH 8 is unclear. At pH 10, the YSZ suspension, as at pH 6, shows no clarification, possibly related to the breakage of the large ~0.95 µm agglomerates from pH 8 into ~0.40 µm ones at pH 10. As the clarification thickness is controlled by the smaller particle size, the suspensions at pH 6 and 10 appear to have the same sedimentation behavior. Meanwhile, the PS suspensions present the same clarification rate at pHs 8 and 10. Applying Stokes' law with dynamic viscosity of water $\mu = 0.001$ kg (m s)$^{-1}$, the sedimentation velocity of 1 mm h^{-1} was calculated for the PS spheres (density of 1050 kg m^{-3}), which matches precisely the clarification rate of the PS at pH 8 and 10. In the case of YSZ agglomerates, the sedimentation velocity cannot be calculated as easily because the density of the agglomerates is not known. If the sedimentation rate measured by the clarification rate (0.6 mm h^{-1}, at pH 8) is used to back calculate the effective density of the agglomerates, 1340 kg m^{-3} is found to be the final density.

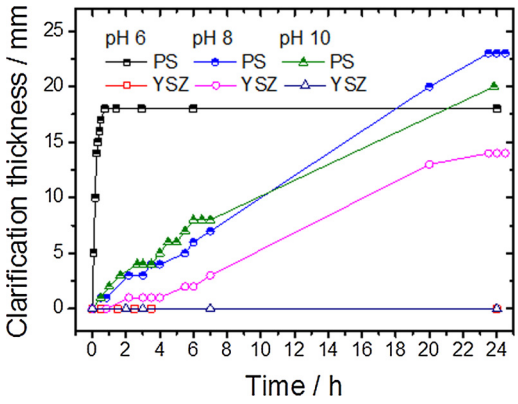

Fig. 3. Clarification thickness (mm) versus time (h) for PS and YSZ at different pHs.

3.2. DLVO calculations

DLVO theory can help to understand the particle-particle interactions in this system. Fig. 4 shows the interaction free energy (U) normalized by the ambient thermal energy (k_BT) with $T = 298$ K versus the separation distance for the three pHs tested experimentally. Although the theory is only quantitatively valid for $\Psi < \pm 25$ mV, various studies claim a good approximation for higher surface potentials up to ± 40 mV [28–30]. Here, we aim to describe the interaction behavior qualitatively. The systems can be described as oppositely charged (a), charged-neutral (b) and similarly charged (c) systems, when the particle-pairs have the opposite surface charge, have one charged and one neutral particle and have the same surface charge, respectively. All three cases in this study are asymmetric systems, i.e. the magnitudes of the surface charges are not comparable. At pH 6, the system is asymmetrically oppositely charged and, as expected, present attractive energies for all boundary conditions. The attractive interactions found in the calculations explain the PS-YSZ core-shell structures created in suspension. At pH 10, the system is asymmetrically similarly charged and presents repulsive forces at long distances due to the double layer and attractive forces at very short distances due to van der Waals forces for all boundary conditions. The repulsive interactions at long distances assures that no PS-YSZ core-shell structures are created in suspension. The pH 8 presents the more complex situation of a charged-neutral system, where the boundary conditions become extremely important. In this case the CC conditions predict repulsive energies down to separation distances of a few nanometers and the CP conditions give an attractive behavior over the whole separation distance. In the charged-neutral case the forces are highly sensitive to the CR. The interaction between PS spheres was already experimentally observed, and showed that the CR condition often better represents the case of real interactions [24,25]. If the CR condition (with $p = 0.5$) represent the present case, neither attractive nor repulsive interactions are found at long distances and at very short distances attractive interactions take place due to van der Waals forces. This means that there are no interactions between the PS and YSZ particles until they come into contact. The corresponding force profiles of these asymmetric systems are comparable with previous calculations [23] and can be found in the Electronic

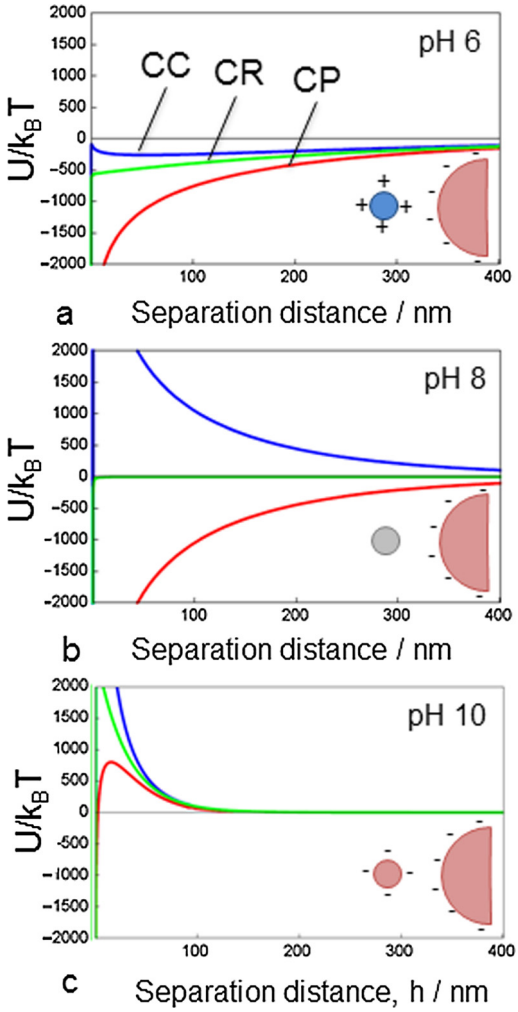

Fig. 4. Interaction free energy (U) normalized by k_BT versus the separation distance between two differently charged colloidal particles predicted by DLVO for the PS-YSZ system at a) pH 6, b) pH 8 and c) pH 10. The DLVO with CC, CP, and CR boundary conditions are shown. The insets present the schematic of particles and surface charges for each situation, in which the PS particles are represented with a half sphere and the YSZ particles as a full sphere.

Supplementary Information Figure S1.

3.3. Effect of pH on film microstructure

To study the effect of pH on the PS-YSZ mixtures, suspensions with a 2.5 YSZ/PS ratio by weight were formulated and the pH adjusted to 6, 8 and 10. Films were prepared by drop-casting the suspensions, followed by calcination at 500 °C for 30 min to eliminate the PS spheres and produce the inverted structures. Fig. 5 shows SEM images at low and high magnification of the resulting structure of the films deposited at different pHs.

At pH 6, heterocoagulation takes place and PS-YSZ core-shell structures are formed in suspension. The excess of YSZ particles, which cannot be heterocoagulated, form a separate phase inside the film. As can be observed in Fig. 5a, the nature of the suspension results in two different and distinct areas in the deposited films: regions consisting of YSZ-shells related to the heterocoagulation (right side of image) and regions of free YSZ nanoparticles (left side of image). The shape of the YSZ-shells after inversion is clearly visualized at higher magnification (Fig. 5b).

At pH 8, the YSZ nanoparticles agglomerate up to sizes of ~0.95 µm, which gives rise to a situation in which the sedimentation rates of the PS and YSZ match, as discussed previously. The resulting microstructure of the films (Fig. 5c and 5d) does not exhibit YSZ-shells, but rather an infiltrated array of pores. This was confirmed by cross-section analysis of the film (Fig. 6a), which showed a high homogeneity through the entire film thickness. Some of the pores are not open on the surface, which can be accounted for the small amount of smaller ~0.15 µm agglomerated YSZ that sediments slower than the bigger agglomerates. This microstructure is found to be ideal for the application we seek. Instead of increasing the amount of YSZ in the structure by attempting to increase the degree of heterocoagulation, i.e final shell thickness, we succeeded in depositing an infiltrated inverse photonic glass by tuning the YSZ nanoparticle surface charge in a way that these nanoparticles coagulate to approx. 1 µm sized agglomerates and therefore sediment as fast as the 3 µm sized PS particles. Depositing under charged-neutral rather than oppositely charged conditions resulted in a more filled structure, with better optical properties. The reflectance behavior of this structure is presented later in this manuscript.

Lastly, Fig. 5e and f show the microstructure of films deposited from the suspension at pH 10. As seen in the cross-section (Fig. 6b), the bulk of the film exhibits a microstructure comparable to the one at pH 8, but containing an additional layer of only YSZ nanoparticles on the region near to the free surface. The reason for these two different layers is the two different YSZ agglomerate sizes at pH 10. The lower layer is the result of YSZ agglomerates with sizes of ~0.95 µm sedimenting at rates comparable to the PS, similar to the effect at pH 8. However, the upper layer is the result of the additional volume fraction of smaller agglomerates of ~0.4 µm at pH 10. These sediment much slower and end up as a separate layer on top of the film.

3.4. Effect of YSZ/PS ratio on film microstructure

Further experiments were carried out at pH 6 to evaluate the limits of heterocoagulation in this system. For that purpose, films deposited from suspensions of YSZ/PS ratios by weight of 0.2, 0.3, 0.4, 0.5, 1.0, 1.5, 2.0 and 2.5 were produced. Fig. 7 shows representative microstructures of these films before calcination, i.e. still containing PS. At 0.2 YSZ/PS ratio (Fig. 7a), the PS spheres are not completely coated and thereby, are not suitable for inversion. At 0.3 YSZ/PS ratio (Fig. 7b), the PS spheres are completely coated and an almost undetectable amount of free YSZ is present at the edge of the sample. At ratios greater than 0.3 YSZ/PS, areas containing only free YSZ-nanoparticles are observed, i.e. the film structure is not homogeneous. Fig. 7c shows an example of such an area with large amount of free YSZ (left frame) and one area where complete heterocoagulation occurred (right frame). A larger magnification of the area of complete heterocoagulation can be seen in Fig. 7d. The limit found in this system is much lower than what was previously observed for 0.756 µm PS spheres [4]. In the former, suspensions with a ratio of 2.5 of YSZ/PS still presented complete heterocoagulation, i.e. there was no formation of areas containing only YSZ-nanoparticles.

As the conditions at pH 8 resulted in a more ideal and filled structure (see Figs. 5c-d and Fig. 6a), the influence of the YSZ concentration on the sedimentation behavior and, later, the photonic properties of the resultant structures was assessed. As above, the YSZ/PS ratio was varied from 0.3 to 2.5 also for samples deposited at pH 8. Fig. 8 shows the strong differences between the films when using YSZ/PS ratios of 0.3 − 0.5 and 1.0 − 2.5. Fig. 8a and b show that for low YSZ concentrations (6–10 mg mL^{-1}) the films show phase separation between YSZ and PS. The PS forms a bottom layer and the YSZ an upper layer. Strong delamination occurs at these low concentrations, due to a higher shrinkage of the upper YSZ layer during drying, which results in delamination and pulling off of some PS spheres from the lower layer. Conversely, Fig. 8c-f show that stable films are achieved for higher YSZ concentrations (20–50 mg mL^{-1}). The microstructures are comparable across this concentration range and are consistent with the structures discussed previously at Fig. 5c and d (2.5 YSZ/PS ratio at pH 8).

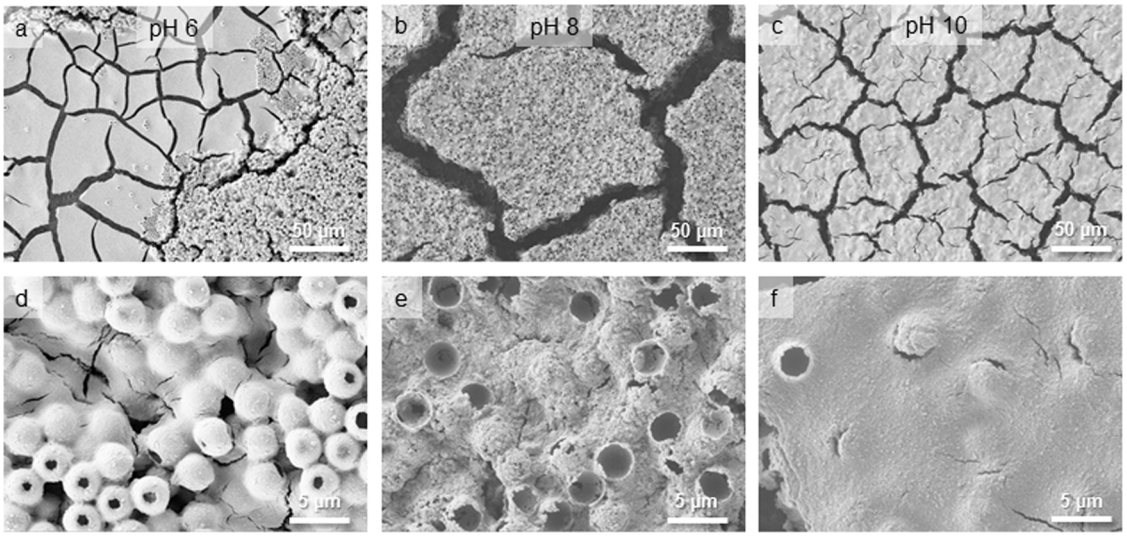

Fig. 5. SEM surface images of films deposited from suspensions with 2.5 YSZ/PS ratio by weight at a/b) pH 6, c/d) pH 8 and e/f) pH 10. Structures were calcined at 500 °C for 30 min to eliminate the PS template.

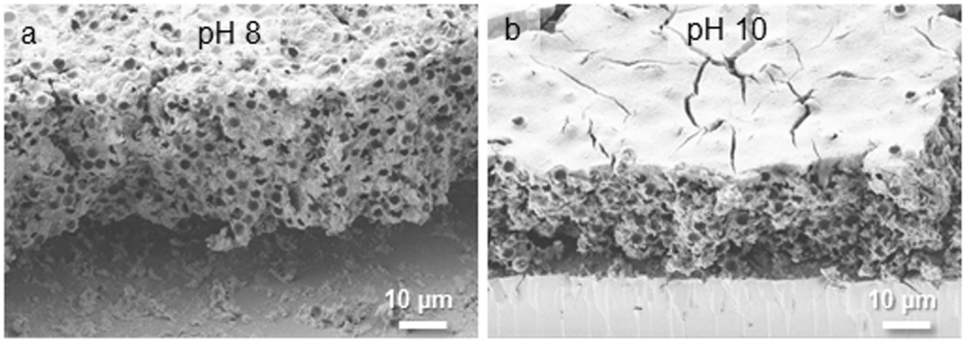

Fig. 6. SEM cross-section images of films deposited from 2.5 YSZ/PS ratio by weight suspensions at a) pH 8 and b) pH 10. Structures were calcined at 500 °C for 30 min to eliminate the PS template.

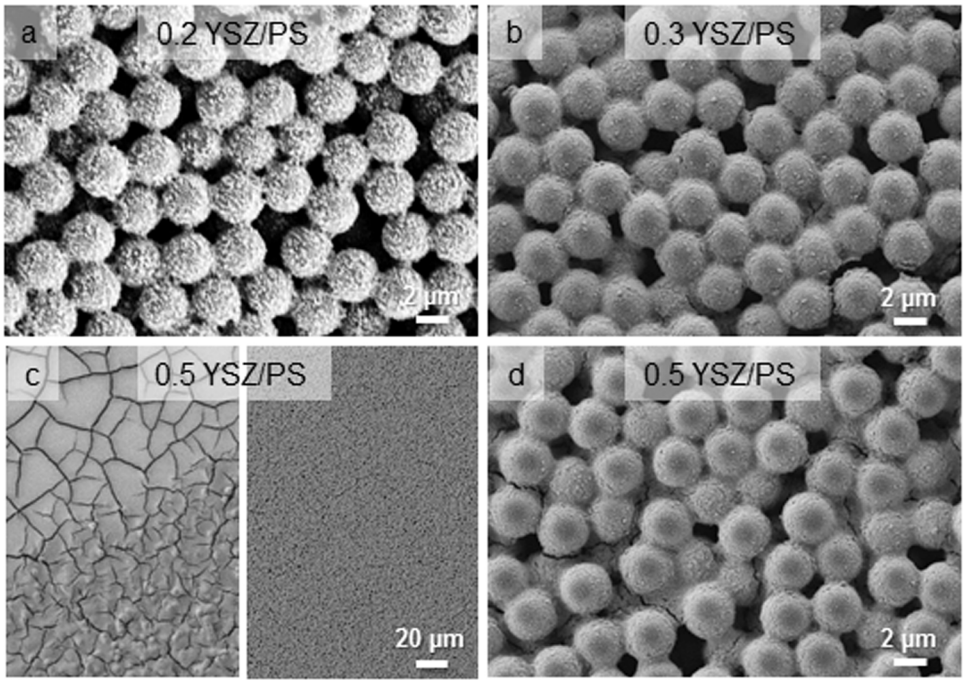

Fig. 7. SEM surface images of films deposited from suspensions at pH 6 with a) 0.2, b) 0.3 and c/d) 0.5 YSZ/PS ratios by weight. Images show different regions of free YSZ (c[left]: low magnification) and heterocoagulation (c[right]: low magnification, d: high magnification). The structures still contain the PS template.

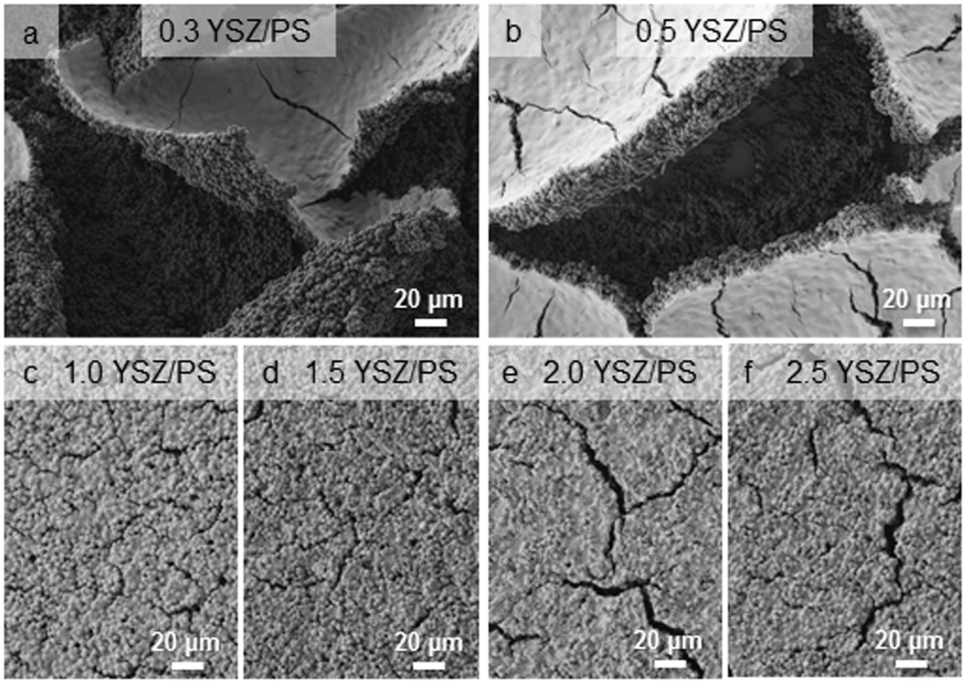

Fig. 8. SEM surface images of films deposited from suspensions at pH 8 with a) 0.3, b) 0.5, c) 1.0, d) 1.5, e) 2.0, and f) 2.5 YSZ/PS ratios by weight. Delamination observed for 0.3 and 0.5 YSZ/PS. Structures still contain the PS template.

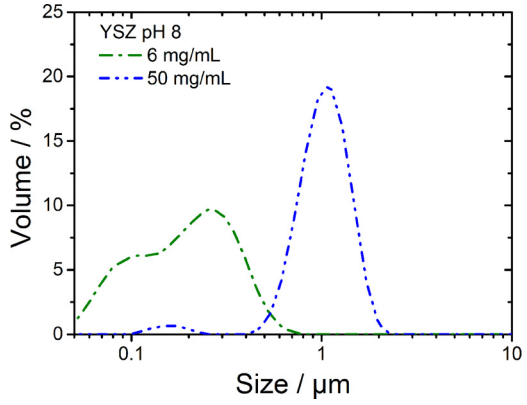

Fig. 9. Particle size distribution: Volume (%) versus particle size (µm) for YSZ suspensions at pH 8 for two different concentrations.

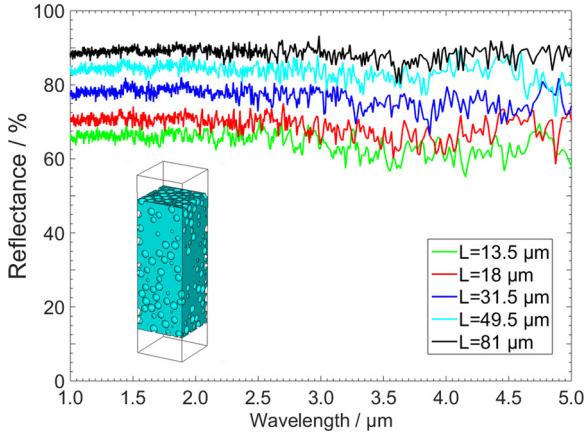

Fig. 10. Calculated hemispherical diffuse reflection from inverse YSZ photonic glass according to the different film thicknesses and a diameter of air spheres of 3 µm. The inset shows the schematic drawing of the simulated structure.

To understand the phase separation between YSZ and PS at lower YSZ concentrations, particle size analysis (Fig. 9) at different YSZ concentrations was carried out. At high YSZ concentrations (2.5 YSZ/PS ratio, 50 mg mL^{-1}), agglomeration results in the majority of the particles being ~0.95 µm. However, if the concentration of YSZ is reduced to the one used in the 0.3 YSZ/PS ratio (6 mg mL^{-1}), no further agglomeration at pH 8 was observed. The particle size measurements at pH 8 indicate almost identical sizes as at pH 6 as already shown in Fig. 2 (peaks at ~0.10 µm and ~0.25 µm). This accounts for the formation of the upper YSZ layer, as low concentrations result in smaller YSZ agglomerates that have a larger mismatch in sedimentation rates compared to the PS spheres. Therefore, we conclude that when depositing under charge-neutral conditions, controlling solid-concentration plays a critical role in the formation of agglomerates and thus determines the sedimentation rates and must be considered in order to achieve highly filled structures.

3.5. Optical simulations

Fig. 10 shows the calculated reflectance of an inverse YSZ photonic glass with spherical pore sizes of 3 µm (see inset in Fig. 10) with varying film thicknesses (L) between 13 and 81 µm. The light was excited from air at the top and transmission at the bottom was calculated. The hemispherical diffuse reflection of such a system can be obtained by $R = 1 - T$, where R is the hemispherical diffuse reflection and T is the hemispherical diffuse transmission, assuming no absorptivity of YSZ for wavelengths ranging from 1–5 µm. Simulations indicate that high reflection efficiencies in a wavelength range of 1–5 µm can be expected for inverse YSZ photonic glasses with air spheres of 3 µm diameter. The transmission follows the typical inverse law for diffuse scattering $T \sim \frac{1}{L}$. Thus, to increase the reflection e.g. from 80% to 90% an increase in the film thickness is required. The scattering strength of photonic glass drops significantly above cutoff wavelength. It can be approximated as double pore diameter times the average refractive index $2Dn_{av}$ and it corresponds to the condition when half of the effective wavelength fits between the centers of two neighboring pores. For the considered pores of 3 µm the cut off wavelength is significantly beyond 5 µm.

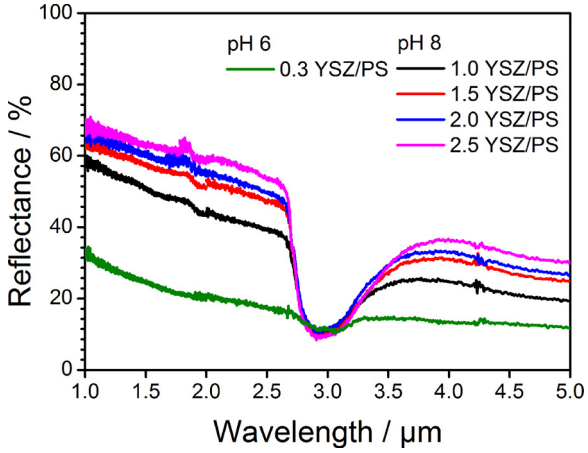

Fig. 11. Reflectance spectra of YSZ inverse photonic glasses deposited at pH 6 and pH 8 according to the different YSZ/PS ratios (0.3, 1.0, 1.5, 2.0 and 2.5).

3.6. Photonic properties

Diffuse reflectance spectra (Fig. 11) were measured to evaluate the influence of the shell-like versus infiltrated structures on the photonic behavior. The omnidirectional broad-band reflectance arises from the multiple scattering in the structure. All spectra show a reflectance dip at wavelengths of 2.75–4.00 µm due to the absorption of OH groups on the YSZ surface. This absorption dip was previously observed for YSZ-based TBC systems [31–33] and direct photonic glasses fabricated from undoped and doped zirconia [5,6]. Its contribution is expected to disappear at high temperature operation, as in the case of TBCs. Small noise at 4.2 µm corresponds to slight changes of the CO_2 concentration in the optical path of the FTIR-spectrometer between sample and reference measurements.

The reflectance spectrum for the photonic glasses with shell structures deposited at the heterocoagulation limit (0.3 YSZ/PS ratio, pH 6) shows a very low reflectance between 30 and 15%. As noted in the previous section, higher concentrations of YSZ cannot be incorporated at this pH value for the given PS size, hence phase separation occurs. Moreover, the film thickness was only 20 ± 2 µm, corresponding to approximately six-fold the polymer template size, which also results in low scattering. These results indicate that heterocoagulation becomes a less effective method to fabricate inverse photonic glasses for applications at longer wavelengths where large template sizes are needed, such as in thermal reflectors and barrier coatings, due to the lower concentration limits. Heterocoagulation in the studied YSZ/PS system corresponds to the condition in which the particles have opposite charges (Fig. 4a) and differs therefore, from the sedimentation mechanism at pH 8 where the particles are in a neutral-charged condition, for YSZ and PS respectively (Fig. 4b).

Conversely to the condition observed at pH 6, at pH 8 the YSZ/PS ratio in the deposited films could be varied over a higher amount from 1.0–2.5. The thicknesses were measured to be 33 ± 4, 28 ± 2, 31 ± 5 and 32 ± 3 µm for 1.0, 1.5, 2.0 and 2.5 YSZ/PS samples, respectively. It can be observed that the reflectance increases with increasing YSZ content, varying from ~58% to ~68% at wavelength of 1 µm. The magnitude of reflectance is more than twice that achieved using heterocoagulation. Even when accounting for their larger thicknesses, the fully infiltrated structures still outperform the heterocoagulated structure. This is due to the increased fraction of high refractive index material in the infiltrated structures. The reflectivity is still lower than the simulated values though (Fig. 10). This can be attributed to the fact that the obtained YSZ inverse photonic glasses consist of agglomerated nanoparticles which are not a fully dense material and thereby, the effective refractive index is smaller than 2.12.

The scattering properties of TBCs are becoming more and more important as the work temperature of engines increases [34]. The radiative properties of such coatings are being investigated [31–37] and the concept of optimizing TBCs for high reflectance was already applied for common fabrication processes such as air plasma spraying (APS) [35] and electron beam physical vapor deposition (EB-PVD) [36,37]. For example, APS allows microstructural modification with features like pores and microcracks [35], and EB-PVD with features like pores and orientation of the feathery microstructure for scattering enhancement [36]. Nevertheless, in these works the enhancement of the scattering properties by microstructural features only increased the reflectance intensity in the near- (0.75–1.4 µm) and short-wavelength (1.4–3 µm) infrared range, while at our work the reflectance is maintained for a wider wavelength range (1–5 µm).

The application of inverse photonic glasses in TBC systems is not proposed to directly substitute the current systems, but rather as a possibility of an additional layer to decrease radiative heat transport. Furthermore, the films fabricated in this work can be used as broadband omnidirectional reflectors in general.

3.7. High-temperature behavior

The thermal stability of the photonic glasses was evaluated by assessing the microstructural changes (Fig. 12) and reflection behavior (Fig. 13) as a function of temperature and time. Samples with very diverse microstructures, i.e. 0.3 YSZ/PS deposited at pH 6 and 2.5 YSZ/PS deposited at pH 8, were exposed to high temperatures up to 1200 °C for a total of 120 h. The structures generated by heterocoagulation (0.3 YSZ/PS, pH 6) maintained their shape up to 1200 °C for 4 h, with distortion and loss of the spherical pore shape when further annealed. On the other hand, infiltrated structures (2.5 YSZ/PS, pH 8) maintained their structural integrity (spherical pores) up to 1200 °C for 120 h. Micrographs for all tested temperatures can be found in Figure S2 at the Supplementary Information.

With regards to the reflectance behavior (Fig. 13), the fully infiltrated inverse photonic glasses generated at pH 8 presented overall higher reflectance values than the shell-like structures fabricated by heterocoagulation at pH 6. This can be associated both to the higher film thicknesses achieved by this route (32 vs. 20 µm, in average), but mainly to the presence of more YSZ particles in the structure (2.5 against 0.3 YSZ/PS ratio). As expected, the OH absorption peak (2.75–4.00 µm) becomes less pronounced with increasing temperature and time for both types of structures, as these functional groups desorb at high temperatures.

The structures generated by heterocoagulation (Fig. 13a) show an increase in reflectance at shorter wavelengths with increased annealing temperature and time. This can be related to the structural changes observed in the micrographs. After the heat treatment performed at 1000 °C, a clear flattening of the shell's surface can be observed (compare the structures after 500 °C and 1000 °C). As the shells are formed by nanoparticles, they have a high driving force for sintering [38] which shall lead to densification of the shells and thereby, to an increase of the shells effective refractive index. As discussed previously, the refractive index is linked to the reflectance capability of the photonic glass. However, the level of densification is restricted by the very open structure (initial macro porosity > 40% [39,40]) and after heat treatment at 1200 °C for 120 h, the shells collapse and an intricated structure is formed (Fig. 12, left column). This collapse leads to a decrease in the reflectance, when compared to the previous heat treatment condition (1200 °C for 4 h). In an overall view, the whole structure seems to de-sinter.

Local densification is also expected to occur for the infiltrated structures (Fig. 12, right column), but in this case the amount of YSZ-particles per volume is much higher (2.5 against 0.3 YSZ/PS) and therefore, the OH-absorption component is expected to be higher (compare the peak width and depth from Fig. 13a and b), as there is more surface per volume available for OH groups adsorption. The

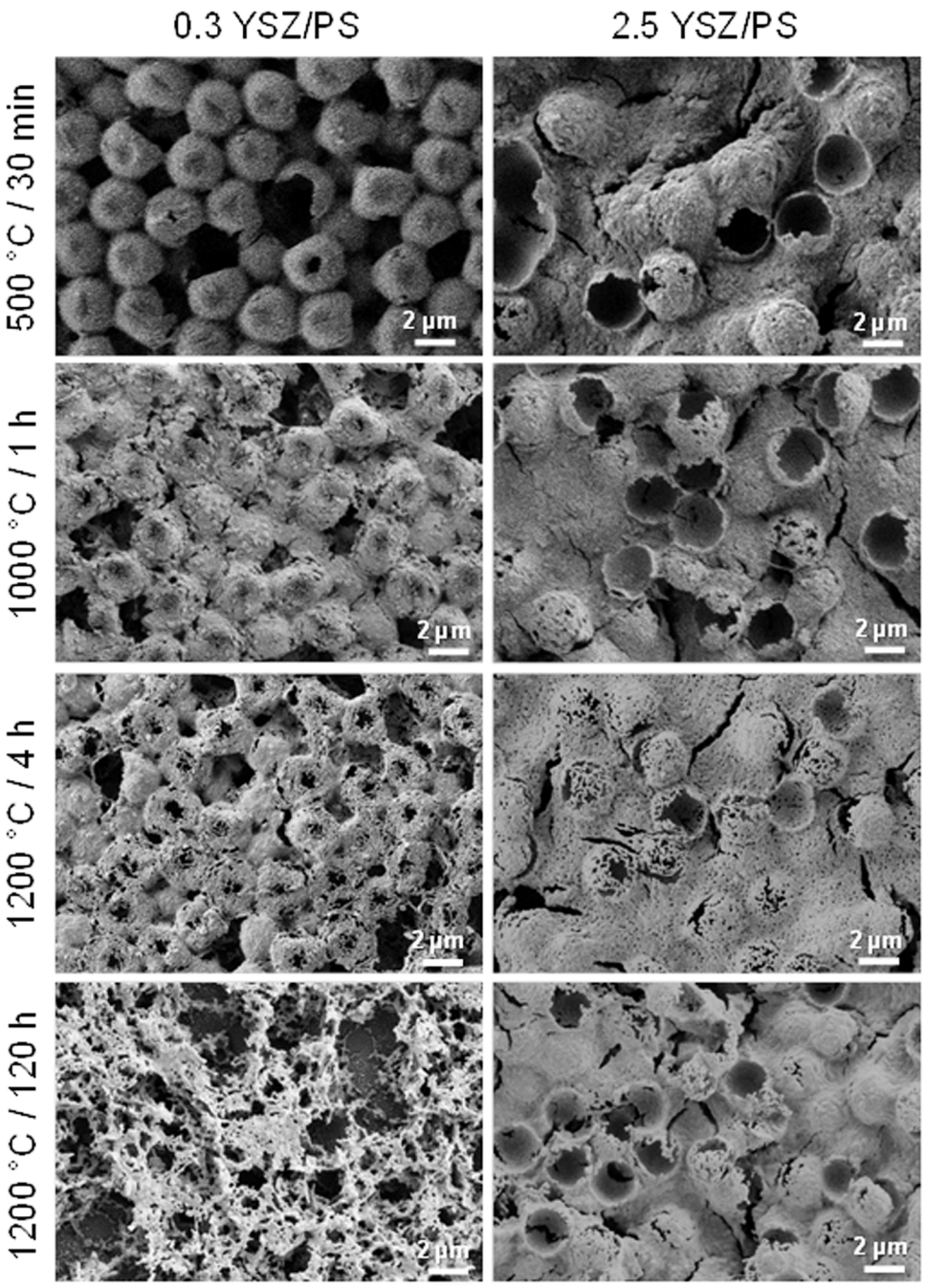

Fig. 12. SEM images of the layer with 0.3 YSZ/PS (left) and 2.5 YSZ/PS (right) after different heat treatments.

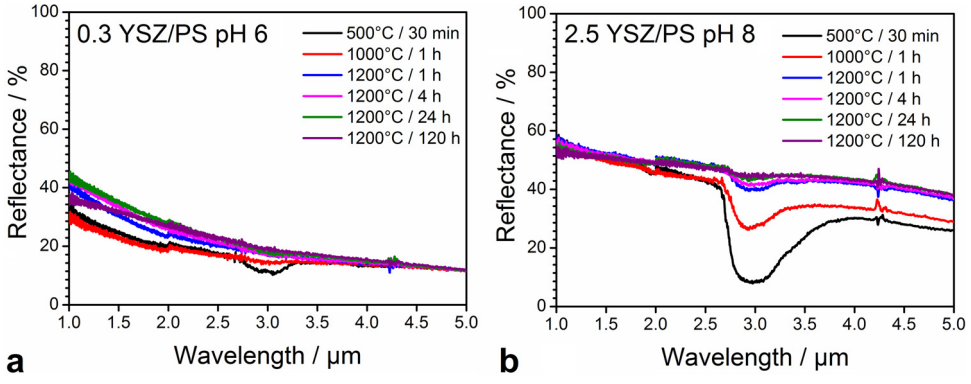

Fig. 13. Reflectance spectra of photonic glasses after different heat treatments for a) 0.3 YSZ/PS deposited at pH 6 and b) 2.5 YSZ/PS deposited at pH 8.

significant increase in the reflectance at longer wavelengths (> 3.00 μm) is attributed to the YSZ particles area densification, as well as the elimination of OH groups at high temperatures, as OH absorption is relatively high in the mid infrared region. As the source of absorption in the structures is eliminated, the spectra approximate to the simulated one showed at Fig. 10, corresponding to a stable reflectance value over the wavelength range (1–5 μm). More importantly, the infiltration-based photonic glasses maintained their high reflectance for all the heat-treatment conditions and even after exposure at 1200 °C for 120 h.

When in comparison to ordered structures (inverse opal photonic crystals), the photonic glasses produced at this work performed quite well. Zhang et al. [41], for example, reported structures of $La_{0.8}Sr_{0.2}MnO_3$/YSZ that were stable only up to 1100 °C when conventionally heat treated. YSZ structures were also produced by Lashtabeg et al. [42], for which sintering and accentuated grain growth are visible already for heat-treatments performed at 1100 °C for 5 h, with apparent loss of the macro pores spherical shape. The performance of our photonic glasses is highlighted in a further comparison with other ceramics materials, namely SiO_2 [43], TiO_2 [43,44] and Al_2O_3 [45] photonic crystal structures. For a sol-gel infiltration route [43], partial collapse of both SiO_2 and TiO_2 structures was observed already after heat treatment at 850 °C for 4 h. An atomic layer deposition (ALD) route improved the stability of TiO_2 structures [44] up to 1000 °C for 4 h, however significant grain growth was observed. For ALD-based Al_2O_3 [45] structures, a stability up to 1200 °C is reported, but the samples were heat treated only for 1 h. In this work, the structures were heat treated up to 120 h at 1200 °C having its reflectance capability maintained after the heat treatments.

Additionally, the crack area fraction was found to increase mostly with the temperature (Figure S4). For the heterocoagulation-based photonic glasses (0.3 YSZ/PS), cracks are originated during drying of the deposited films, but also during the heat treatments, as can be observed in Fig. 12 when comparing the samples heat-treated at 1200 °C to 4 h and 120 h. In the case of the infiltrated structures (2.5 YSZ/PS), the area fraction of cracks starts at ~4% for the as-deposited structure, increasing to ~17% for inverted structures and later on to ~35% at 1200 °C. An increase in the heat-treatment dwell time from 1 h to 120 h led to an increase in area fraction of only 2%. Lower magnification micrographs and a plot of the area fraction of cracks for the infiltrated structures after various heat treatments can be found in the Electronic Supplementary Information Figures S3 and S4.

As expected for zirconia doped with 8 mol% yttria, the material stays in the cubic phase (ICDD PDF 30–1468) after all heat treatments. XRD spectra of the photonic glasses can be found in the Electronic Supplementary Information Figure S5.

4. Conclusions

An all-colloidal route to produce YSZ inverse photonic glasses was explored. The behavior of the base materials and suspensions was characterized with respect to their charges, particle sizes, and sedimentation rates as a function of pH, and the effects on film microstructure were determined. At pH 6, opposing charges of the YSZ and PS resulted in heterocoagulation and yielded thin shell structures after inversion. Above a critical YSZ concentration which depends on the PS size, areas with free YSZ particles were formed. At pH 8, uncharged YSZ nanoparticles agglomerated, which gave rise to a situation in which the sedimentation rates of the PS and YSZ matched. Depositing under uncharged rather than oppositely charged conditions resulted in a more filled and ideal structure. The particle interactions were consistent with DLVO and sedimentation models and accounted for the differences in microstructure. Photonic glasses deposited under sedimentation conditions at pH 8 allowed a higher amount of YSZ particles incorporation, resulting in higher reflectance up to ~68% at a wavelength of 1 μm. While heterocoagulated-based photonic glasses were only stable up to 1200 °C for 4 h, the more infiltrated structures remained stable after heating at 1200 °C for up to 120 h, which enables its use in high-temperature photonic applications.

Acknowledgements

Funded by the Deutsche Forschungsgemeinschaft (DFG, German Research Foundation) – Projektnummer192346071 – SFB 986.

Appendix A. Supplementary data

Supplementary material related to this article can be found, in the online version, at doi:https://doi.org/10.1016/j.jeurceramsoc.2019.04.028.

References

[1] P.D. García, R. Sapienza, Á. Blanco, C. López, Photonic glass: a novel random material for light, Adv. Mater. 19 (2007) 2597–2602, https://doi.org/10.1002/adma.200602426.
[2] P.D. García, R. Sapienza, C. López, Photonic glasses: a step beyond white paint, Adv. Mater. 22 (2010) 12–19, https://doi.org/10.1002/adma.200900827.
[3] S. Gottardo, R. Sapienza, P.D. García, A. Blanco, D.S. Wiersma, C. López, Resonance-driven random lasing, Nature Photon 2 (2008) 429–432, https://doi.org/10.1038/nphoton.2008.102.
[4] J.J. do Rosário, P.N. Dyachenko, R. Kubrin, R.M. Pasquarelli, A.Y. Petrov, M. Eich, G.A. Schneider, Facile deposition of YSZ-Inverse photonic glass films, ACS Appl. Mater. Interfaces 6 (2014) 12335–12345, https://doi.org/10.1021/am502110p.
[5] P.N. Dyachenko, J.J. do Rosário, E.W. Leib, A.Y. Petrov, R. Kubrin, G.A. Schneider, H. Weller, T. Vossmeyer, M. Eich, Ceramic photonic glass for broadband omnidirectional reflection, ACS Photonics 1 (2014) 1127–1133, https://doi.org/10.1021/ph500224r.
[6] E.W. Leib, R.M. Pasquarelli, J.J. do Rosário, P.N. Dyachenko, S. Döring, A. Puchert, A.Y. Petrov, M. Eich, G.A. Schneider, R. Janssen, H. Weller, T. Vossmeyer, Yttria-stabilized zirconia microspheres: novel building blocks for high-temperature photonics, J. Mater. Chem. C Mater. Opt. Electron. Devices 4 (2016) 62–74, https://doi.org/10.1039/C5TC03260A.
[7] S. Magkiriadou, J.-G. Park, Y.-S. Kim, V.N. Manoharan, Absence of red structural color in photonic glasses, bird feathers, and certain beetles, Phys. Rev. E Stat. Nonlin. Soft Matter Phys. 90 (2014) 62302, https://doi.org/10.1103/PhysRevE.90.062302.
[8] N. Vogel, S. Utech, G.T. England, T. Shirman, K.R. Phillips, N. Koay, I.B. Burgess, M. Kolle, D.A. Weitz, J. Aizenberg, Color from hierarchy: diverse optical properties of micron-sized spherical colloidal assemblies, Proc. Natl. Acad. Sci. U. S. A. 112 (2015) 10845–10850, https://doi.org/10.1073/pnas.1506272112.
[9] Y. Zhang, B. Dong, A. Chen, X. Liu, L. Shi, J. Zi, Photonics: using cuttlefish ink as an additive to produce non-iridescent structural colors of high color visibility (adv. Mater. 32/2015), Adv. Mater 27 (2015) 4666, https://doi.org/10.1002/adma.201570213.
[10] V. Shklover, L. Braginsky, G. Witz, M. Mishrikey, C. Hafner, High-temperature photonic structures. thermal barrier coatings, infrared sources and other applications, J. Comp. Theo Nano 5 (2008) 862–893, https://doi.org/10.1166/jctn.2008.2532.
[11] H.S. Lee, R. Kubrin, R. Zierold, A.Y. Petrov, K. Nielsch, G.A. Schneider, M. Eich, Thermal radiation transmission and reflection properties of ceramic 3D photonic crystals, J. Opt. Soc. Am. B 29 (2012) 450–457, https://doi.org/10.1364/JOSAB.29.000450.
[12] R. Kubrin, H.S. Lee, R. Zierold, A.Y. Petrov, R. Janssen, K. Nielsch, M. Eich, G.A. Schneider, Stacking of ceramic inverse opals with different lattice constants, J. Am. Ceram. Soc. 95 (2012) 2226–2235, https://doi.org/10.1111/j.1551-2916.2012.05156.x.
[13] Q. Yan, L.K. Teh, Q. Shao, C.C. Wong, Y.-M. Chiang, Layer transfer approach to opaline hetero photonic crystals, Langmuir 24 (2008) 1796–1800, https://doi.org/10.1021/la702668p.
[14] B. Hatton, L. Mishchenko, S. Davis, K.H. Sandhage, J. Aizenberg, Assembly of large-area, highly ordered, crack-free inverse opal films, Nano Lett. 107 (2010) 10354–10359, https://doi.org/10.1073/pnas.1000954107.
[15] Z. Cai, Y.J. Liu, J. Teng, X. Lu, Fabrication of large domain crack-free colloidal crystal heterostructures with superposition bandgaps using hydrophobic polystyrene spheres, ACS Appl. Mater. Interfaces 4 (2012) 5562–5569, https://doi.org/10.1021/am3014482.
[16] D.-K. Hwang, H. Noh, H. Cao, R.P.H. Chang, Photonic bandgap engineering with inverse opal multistacks of different refractive index contrasts, Appl. Phys. Lett. 95 (2009) 91101, https://doi.org/10.1063/1.3216582.
[17] F. Tang, H. Fudouzi, Y. Sakka, Fabrication of macroporous alumina with tailored porosity, J. Am. Ceram. Soc. 86 (2003) 2050–2054, https://doi.org/10.1111/j.1151-2916.2003.tb03607.x.
[18] Y. Jia, C. Duran, Y. Hotta, K. Sato, K. Watari, Macroporous ZrO2 ceramics prepared from colloidally stable nanoparticles building blocks and organic templates, J. Colloid Interface Sci. 291 (2005) 292–295, https://doi.org/10.1016/j.jcis.2005.04.083.
[19] Y. Jia, C. Duran, Y. Hotta, K. Sato, K. Watari, The effect of polyelectrolyte on

fabrication of macroporous ZrO2 ceramics, J. Mater. Sci. 40 (2005) 2903–2909, https://doi.org/10.1007/s10853-005-2436-3.
[20] B. Derjaguin, L. Landau, Theory of the stability of strongly charged lyophobic sols and of the adhesion of strongly charged particles in solutions of electrolytes, Prog. Surf. Sci. 43 (1993) 30–59, https://doi.org/10.1016/0079-6816(93)90013-L.
[21] B.V. Derjaguin, A theory of the heterocoagulation, interaction and adhesion of dissimilar particles in solutions of electrolytes, Discuss, Faraday Soc. 18 (1954) 85, https://doi.org/10.1039/DF9541800085.
[22] K.J.W. Verwey, J.T. Overbeek, K. van Nes, Theory of the Stability of Lyophobic Colloids: the Interaction of Sol Particles Having an Electric Double Layer, Elsevier, New York, 1948.
[23] G. Trefalt, F.J.M. Ruiz-Cabello, M. Borkovec, Interaction forces, heteroaggregation, and deposition involving charged colloidal particles, J. Phys. Chem. B 118 (2014) 6346–6355, https://doi.org/10.1021/jp503564p.
[24] I. Popa, P. Sinha, M. Finessi, P. Maroni, G. Papastavrou, M. Borkovec, Importance of charge regulation in attractive double-layer forces between dissimilar surfaces, Phys. Rev. Lett. 104 (2010) 228301, https://doi.org/10.1103/PhysRevLett.104.228301.
[25] F.J.M. Ruiz-Cabello, P. Maroni, M. Borkovec, Direct measurements of forces between different charged colloidal particles and their prediction by the theory of Derjaguin, Landau, Verwey, and Overbeek (DLVO), J. Chem. Phys. 138 (2013) 234705, https://doi.org/10.1063/1.4810901.
[26] A.F. Oskooi, D. Roundy, M. Ibanescu, P. Bermel, J.D. Joannopoulos, S.G. Johnson, Meep: a flexible free-software package for electromagnetic simulations by the FDTD method, Comput. Phys. Commun. 181 (2010) 687–702, https://doi.org/10.1016/j.cpc.2009.11.008.
[27] M.N. Bannerman, R. Sargant, L. Lue, DynamO: a free O(N) general event-driven molecular dynamics simulator, J. Comput. Chem. 32 (2011) 3329–3338, https://doi.org/10.1002/jcc.21915.
[28] M. Cerbelaud, A. Videcoq, P. Abélard, C. Pagnoux, F. Rossignol, R. Ferrando, Heteroaggregation between Al 2 O 3 submicrometer particles and SiO 2 nanoparticles: experiment and simulation, Langmuir 24 (2008) 3001–3008, https://doi.org/10.1021/la702104u.
[29] J. Sun, B.V. Velamakanni, W.W. Gerberich, L.F. Francis, Aqueous latex/ceramic nanoparticle dispersions: colloidal stability and coating properties, J. Colloid Interface Sci. 280 (2004) 387–399, https://doi.org/10.1016/j.jcis.2004.08.014.
[30] J. Lee, S.J. Lee, K.H. Ahn, S.J. Lee, Nanoparticle-induced gelation of bimodal slurries with highly size-asymmetric particles: effect of surface chemistry and concentration, Langmuir 31 (2015) 13639–13646, https://doi.org/10.1021/acs.langmuir.5b03752.
[31] G. Yang, C.Y. Zhao, A comparative experimental study on radiative properties of EB-PVD and air plasma sprayed thermal barrier coatings, J. Heat Transfer 137 (2015) 91024, https://doi.org/10.1115/1.4030243.
[32] G. Yang, C.Y. Zhao, B.X. Wang, Experimental study on radiative properties of air plasma sprayed thermal barrier coatings, Int. J. Heat Mass Transf. 66 (2013) 695–698, https://doi.org/10.1016/j.ijheatmasstransfer.2013.07.069.
[33] J.I. Eldridge, C.M. Spuckler, J.R. Markham, Determination of scattering and absorption coefficients for plasma-sprayed yttria-stabilized zirconia thermal barrier coatings at elevated temperatures, J. Am. Ceram. Soc. 92 (2009) 2276–2285, https://doi.org/10.1111/j.1551-2916.2009.03217.x.
[34] D.R. Clarke, M. Oechsner, N.P. Padture, Thermal-barrier coatings for more efficient gas-turbine engines, MRS Bull. 37 (2012) 891–898, https://doi.org/10.1557/mrs.2012.232.
[35] A. Stuke, H. Kassner, J.-L. Marqués, R. Vassen, D. Stöver, R. Carius, Suspension and air plasma-sprayed ceramic thermal barrier coatings with high infrared reflectance, Int. J. Appl. Ceram. Technol. 9 (2012) 561–574, https://doi.org/10.1111/j.1744-7402.2011.02689.x.
[36] G. Yang, C.Y. Zhao, Infrared radiative properties of EB-PVD thermal barrier coatings, Int. J. Heat Mass Transf. 94 (2016) 199–210, https://doi.org/10.1016/j.ijheatmasstransfer.2015.11.063.
[37] D.E. Wolfe, J. Singh, R.A. Miller, J.I. Eldridge, D.-M. Zhu, Tailored microstructure of EB-PVD 8YSZ thermal barrier coatings with low thermal conductivity and high thermal reflectivity for turbine applications, Surf. Coat. Technol. 190 (2005) 132–149, https://doi.org/10.1016/j.surfcoat.2004.04.071.
[38] R. Chaim, M. Levin, A. Shlayer, C. Estournes, Sintering and densification of nanocrystalline ceramic oxide powders: a review, Adv. Appl. Ceram. 107 (2008) 159–169, https://doi.org/10.1179/174367508X297812.
[39] Y. Fu, H. Xie, B. Deng, G. Du, R. Chen, T. Xiao, Three-dimensional structure of polystyrene colloidal crystal by synchrotron radiation X-ray phase-contrast computed tomography, Appl. Phys. A 115 (2014) 781–790, https://doi.org/10.1007/s00339-014-8432-1.
[40] M. Ogurreck, J.J. do Rosario, E.W. Leib, D. Laipple, I. Greving, F. Marschall, A. Last, G.A. Schneider, T. Vossmeyer, H. Weller, F. Beckmann, M. Müller, Determination of the packing fraction in photonic glass using synchrotron radiation nanotomography, J. Synchrotron Radiat. 23 (2016) 1440–1446, https://doi.org/10.1107/S1600577516012960.
[41] N. Zhang, J. Li, W. Li, D. Ni, K. Sun, High performance three-dimensionally ordered macroporous composite cathodes for intermediate temperature solid oxidefuel cells, RSC Adv. 2 (2012) 802–804, https://doi.org/10.1039/C1RA00837D.
[42] A. Lashtabeg, J. Drennan, R. Knibbe, J.L. Bradley, G.Q. Lu, Synthesis and characterisation of macroporous Yttria stabilised Zirconia (YSZ) using polystyrene spheres as templates, Microporous Mesoporous Mater. 117 (2009) 395–401, https://doi.org/10.1016/j.micromeso.2008.07.018.
[43] F. Tang, T. Uchikoshi, Y. Sakka, A practical technique for the fabrication of highly ordered macroporous structures of inorganic oxides, Mater. Res. Bull. 41 (2006) 268–273, https://doi.org/10.1016/j.materresbull.2005.08.021.
[44] R.M. Pasquarelli, H.S. Lee, R. Kubrin, R. Zierold, A.Y. Petrov, K. Nielsch, G.A. Schneider, M. Eich, R. Janssen, Enhanced structural and phase stability of titania inverse opals, J. Eur. Ceram. Soc. 35 (2015) 3103–3109, https://doi.org/10.1016/j.jeurceramsoc.2015.04.041.
[45] K.P. Furlan, R.M. Pasquarelli, T. Krekeler, M. Ritter, R. Zierold, K. Nielsch, G.A. Schneider, R. Janssen, Highly porous α-Al_2O_3 ceramics obtained by sintering atomic layer deposited inverse opals, Ceram. Int. 43 (2017) 11260, https://doi.org/10.1016/j.ceramint.2017.05.176.F30-1468.